



## Article

# Inversion of Soil Moisture on Farmland Areas Based on SSA-CNN Using Multi-Source Remote Sensing Data

Ran Wang<sup>1,2,3</sup>, Jianhui Zhao<sup>1,2,3,\*</sup> , Huijin Yang<sup>1,2,3</sup> and Ning Li<sup>1,2,3</sup> <sup>1</sup> College of Computer and Information Engineering, Henan University, Kaifeng 475004, China<sup>2</sup> Henan Key Laboratory of Big Data Analysis and Processing, Henan University, Kaifeng 475004, China<sup>3</sup> Henan Province Engineering Research Center of Spatial Information Processing, Henan University, Kaifeng 475004, China

\* Correspondence: jhzhao@henu.edu.cn

**Abstract:** Soil moisture is a crucial factor in the field of meteorology, hydrology, and agricultural sciences. In agricultural production, surface soil moisture (SSM) is crucial for crop yield estimation and drought monitoring. For SSM inversion, a synthetic aperture radar (SAR) offers a trustworthy data source. However, for agricultural fields, the use of SAR data alone to invert SSM is susceptible to the influence of vegetation cover. In this paper, based on Sentinel-1 microwave remote sensing data and Sentinel-2 optical remote sensing data, a convolution neural network optimized by sparrow search algorithm (SSA-CNN) was suggested to invert farmland SSM. The feature parameters were first extracted from pre-processed remote sensing data. Then, the correlation analysis between the extracted feature parameters and field measured SSM data was carried out, and the optimal combination of feature parameters for SSM inversion was selected as the input data of the subsequent models. To enhance the performance of the CNN, the hyper-parameters of CNN were optimized using SSA, and the SSA-CNN model was built for SSM inversion based on the obtained optimal hyper-parameter combination. Three typical machine learning approaches, including generalized regression neural network, random forest, and CNN, were used for comparison to show the efficacy of the suggested method. With an average coefficient of determination of 0.80, an average root mean square error of 2.17 vol.%, and an average mean absolute error of 1.68 vol.%, the findings demonstrated that the SSA-CNN model with the optimal feature combination had a better accuracy among the 4 models. In the end, the SSM of the study region was inverted throughout four phenological periods using the SSA-CNN model. The inversion results indicated that the suggested method performed well in local situations.

**Keywords:** soil moisture; remote sensing; convolution neural network; sparrow search algorithm; hyper-parameter optimization



**Citation:** Wang, R.; Zhao, J.; Yang, H.; Li, N. Inversion of Soil Moisture on Farmland Areas Based on SSA-CNN Using Multi-Source Remote Sensing Data. *Remote Sens.* **2023**, *15*, 2515. <https://doi.org/10.3390/rs15102515>

Academic Editor: Xianjun Hao

Received: 7 April 2023

Revised: 7 May 2023

Accepted: 9 May 2023

Published: 10 May 2023



**Copyright:** © 2023 by the authors. Licensee MDPI, Basel, Switzerland. This article is an open access article distributed under the terms and conditions of the Creative Commons Attribution (CC BY) license (<https://creativecommons.org/licenses/by/4.0/>).

## 1. Introduction

Surface soil moisture (SSM) is a crucial component of the Earth's ecosystem and actively participates in the water vapor cycle on a global scale [1]. SSM is an essential element for crop development and growth in the agricultural sector. It is also a crucial characteristic for crop growth monitoring, yield estimation, and drought monitoring. Therefore, it is extremely important to obtain accurate and reliable SSM information [2,3].

Although the traditional method of SSM determination by the probe or gravimetric method has high accuracy, it cannot meet the needs of large-scale SSM monitoring. Remote sensing technology has the characteristics of wide coverage and strong aging, becoming the main means of large-scale SSM monitoring at present [4–6].

High spectral and spatial resolution data can be obtained using optical remote sensing. SSM monitoring technology based on optical remote sensing is an indirect way by using visible, near-infrared, and thermal infrared bands. The empirical relationship between

surface parameters and SSM is established by using spectral reflection and radiation characteristics of ground objects to realize SSM inversion [7,8]. By using optical remote sensing data, the vegetation index is extracted in the vegetation coverage area to reduce or remove the impact of vegetation coverage, as to increase the precision of SSM inversion in the vegetation coverage area [9]. However, due to the factor that optical remote sensing is easily affected by the characteristics of the study area, seasonal conditions, and weather conditions, its ability to monitor SSM is limited. Synthetic aperture radar (SAR) with high resolution has been widely used in SSM research because of its all-weather, all-day, high penetrating power and the responsiveness of soil dielectric properties to the radar backscattering coefficient [10]. The radar backscatter coefficient is mainly influenced by factors such as soil dielectric constant, ground surface roughness, and vegetation coverage [11]. Therefore, it is essential to successfully reduce their impact in order to increase the SSM inversion's accuracy. In response to this problem, multi-source remote sensing collaborative inversion of SSM has been widely studied.

To date, researchers have attempted two basic strategies to raise the SSM inversion accuracy. Firstly, classical physical models were used to invert the SSM [12,13]. Secondly, mainstream machine learning techniques were used to maximize the use of different meaningful feature parameters to invert the SSM [14,15].

Considering the penetration capabilities of SAR signals and their sensitivity to the dielectric constant of the surface dielectric constant, a functional model of the backscatter coefficient is typically constructed to estimate the dielectric constant [16,17]. Subsequently, the SSM is calculated using a dielectric mixing model. However, during the SAR ground observation, the interaction mechanisms between vegetation, soil, and electromagnetic waves are complex [18]. Accurately isolating the contributions of vegetation and the surface dielectric constant to radar backscattering is a key focus and challenge in current SAR soil moisture inversion research [19,20].

For SSM inversion on bare ground, Ulaby et al. [21] were the first to suggest that bare soil backscattering depends mainly on surface roughness and soil dielectric constant. Oh, Dobson, Shi et al. [22–24] combined physical models and multi-frequency, multi-polarization or full-polarization data to develop a semi-empirical model for SSM inversion of bare ground. For SSM inversion in vegetated areas, microwave signals from SAR sensors undergo complex interactions between the vegetation and the ground surface, causing the final received backscatter to contain multiple forms of scattered components. It makes SSM estimates potentially inaccurate in vegetated areas. Some scholars had established a series of microwave scattering models by studying the characteristics of microwave scattering, such as the Michigan microwave canopy scattering model (MIMICS) proposed by Ulaby et al. [25] for the inversion of SSM in areas with tall vegetation cover areas and the water cloud model (WCM) proposed by Attema et al. [26] for inversion of SSM in low vegetation covered areas. Zribi et al. [27] combined Sentinel-1 and Sentinel-2 multi-source remote sensing data and developed a SSM inversion model for agricultural land using a normalized difference vegetation index (NDVI) retrieved from Sentinel-2 images and received good inversion results with the precipitation measurements in the study area. EI Hajj et al. [28] combined Sentinel-1 and Sentinel-2 remote sensing data to develop a neural network-based inversion technique to invert radar signals and estimate SSM in vegetated areas. In their study, the combination of WCM and integral equation modeling (IEM) was used to generate a synthetic database. Then, the synthetic database was used to train and validate the neural network. Finally, the trained neural network was used in a real database to evaluate its robustness to SSM estimation. The results showed that SSM could be estimated with an accuracy of about 5 vol.% in agricultural areas.

As an important branch of artificial intelligence, machine learning can integrate multiple elements and learn complex nonlinear mapping relationships. It is increasingly popular in SSM inversion because the number of parameters required for machine learning is not limited by the surface parameters [29,30]. A particular branch of machine learning is known as deep learning [31]. Convolutional neural network (CNN) is a particular class of artificial

neural networks used in deep learning. CNN is renowned for its precise and effective computation, strong learning capacity, and sophisticated feature extraction capability. In recent years, the CNN model has become a highly effective teaching strategy and is widely used in regression fitting analysis [32]. To lessen or eliminate the impacts of scant vegetation in farming regions, Jian Liu et al. [33] constructed a CNN model to extract the deep features from Sentinel-1 and Sentinel-2 remote sensing data and had the optimal inversion accuracy compared with WCM, support vector regression (SVR), and generalized regression neural network (GRNN).

However, the performance of CNN model is sensitive to hyper-parameters, and different settings of hyper-parameters may lead to different generalization capabilities. It is crucial to find the optimal combination of hyper-parameters to enhance the performance of the CNN model. Thus far, researchers have developed numerous optimization algorithms, such as the grey wolf optimizer (GWO) [34], gravitational search algorithm (GSA) [35], and particle swarm optimization (PSO) [36]. Recently, the sparrow search algorithm (SSA) was developed as a result of observations of sparrow populations' foraging and anti-predation behaviors [37]. Compared with benchmark function learning algorithms such as PSO, GWO, and GSA, SSA has stronger optimization capability and faster learning efficiency.

Based on the above analysis, a convolution neural network optimized by the sparrow search algorithm (SSA-CNN) was developed to increase the accuracy of SSM inversion on the surface of agricultural fields. Firstly, multiple feature parameters were extracted from the pre-processed remote sensing images to provide a more comprehensive reference for SSM inversion studies. Then, the correlation analysis of the extracted feature parameters was performed to obtain the best combination of features for SSM inversion. Finally, the SSA-CNN model was proposed for SSM inversion of winter wheat covered farmlands.

The rest of this paper is organized as follows. The study area and the SSM inversion methods are both thoroughly explained in Section 2. The inversion outcomes are displayed in Section 3. There is a discussion and our conclusions in Sections 4 and 5, respectively.

## 2. Materials and Methods

In this paper, a SSM retrieval model combining SSA and CNN was proposed. The vegetation cover type of the study area was winter wheat, and the study period was from October 2019 to February 2021. Section 2.1 briefly describes the study area, and Section 2.2 describes the data used and the preprocessing of the data. Section 2.3 describes the procedure and the methods used in this experiment in detail.

### 2.1. Study Area

The study area was located in Xiangfu District (Lat 34°36'–34°51'N, Lon 114°30'–114°45'E), Kaifeng city, Henan Province, China, which covered an area of approximately 500 km<sup>2</sup>, as shown in Figure 1. The region had a temperate continental monsoon climate and was part of the North China Plain. The climate was ideal for agricultural growth, with an average yearly temperature of about 14 °C and 628 mm of precipitation. The farmland in the research region was mainly planted with winter wheat and corn, and a crop rotation pattern of winter wheat and summer corn was implemented. Winter wheat was generally planted in October and harvested in June of the following year. Four different phenological stages of winter wheat, including the emergence stage, tillering stage, overwintering stage, and standing stage, were selected for SSM inversion during two annual growth cycles of winter wheat, which were 2019–2020 and 2020–2021 cycles.

### 2.2. Data Set and Image Preprocessing

For Sentinel-1 data, Single Look Complex (SLC) format in Interferometric Wide swath (IW) mode and Sentinel-1 Ground Range Detected (GRD) format were used for this study. A total of 10 SAR images acquired on 6 dates was used in the experiment, as shown in Table 1. At first, the Sentinel Application Platform (SNAP) software was used to process SAR images. The GRD data were pretreated by orbit correction, radiometric correction,

multi-looking, speckle filtering using refined Lee filter, and terrain correction. For SLC products, the preprocessing steps were the same as GRD operations except that the filtering operation was polarization filtering. Next, the study area was extracted to extract the feature parameters.

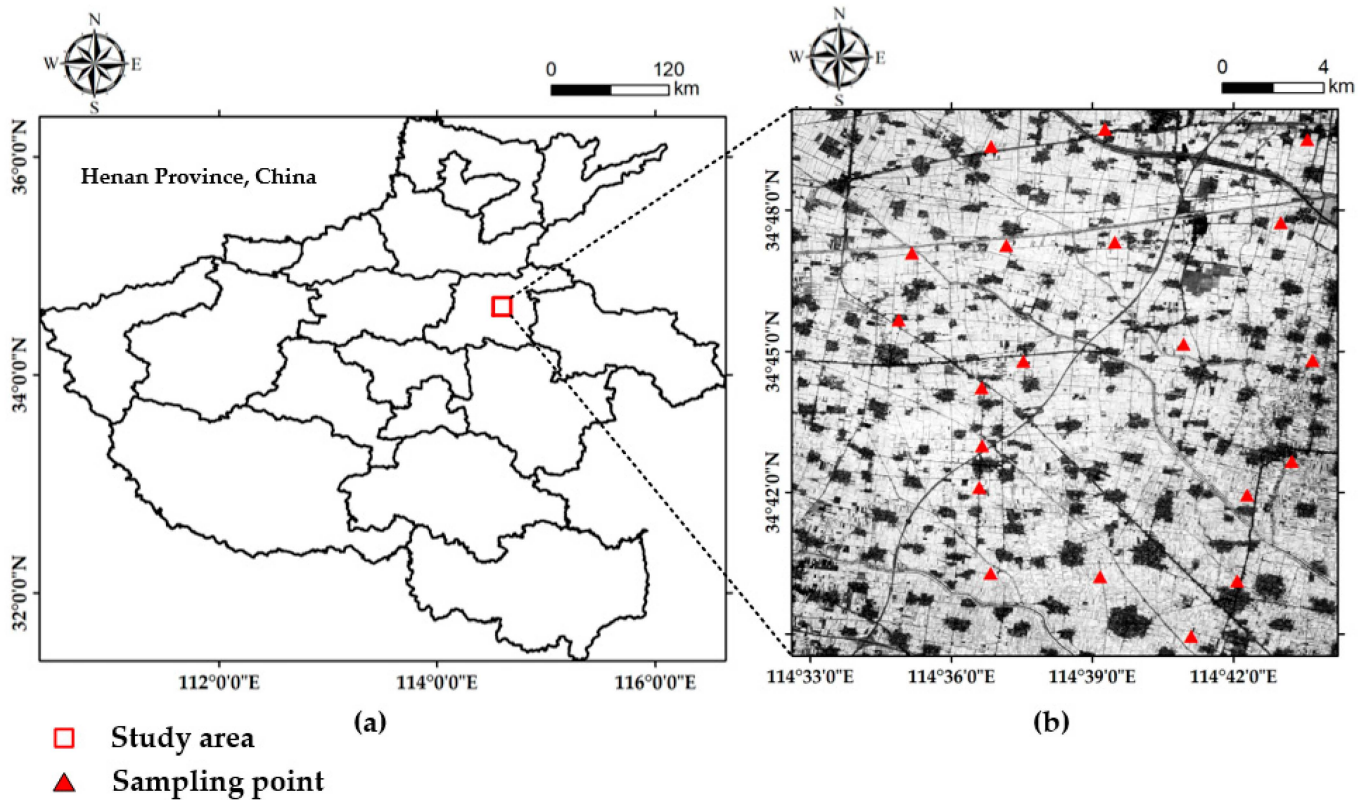


**Figure 1.** Location and Sentinel-1 images of the study area and sampling points: (a) location of the study area; (b) Sentinel-1 image of the study area and sampling points.

**Table 1.** Information of the collected Sentinel-1 data and field measurements.

Acquisition Date of Sentinel-1	Growth Stage	Wheat Height (cm)	SSM Range (Vol.%)
18 October 2019	Emergence	0	6–25
30 October 2019	Tillering	0–5	8–23
29 December 2019	Overwintering	5–15	4–13
22 March 2020	Standing	24–48	2–20
24 October 2020	Emergence	0	7–27
5 November 2020	Tillering	2–8	3–23
11 December 2020	Tillering	4–12	3–12
4 January 2021	Overwintering	6–16	9–29
16 January 2021	Overwintering	6–17	6–13
21 February 2021	Standing	11–21	6–19

The optical data used in this paper were Sentinel-2 Level 2A (L2A) data after atmospheric correction processing. Based on the dates of Sentinel-1 SAR image acquisition and the presence of weather factors such as clouds and rain that affect large fluctuations in soil moisture, 10 quasi-synchronous optical images were selected as experimental data. Band fusion was performed on the downloaded Sentinel-2 images, and then the study area was extracted to calculate the vegetation indexes.

A synchronous ground measurement was carried out on each acquisition date of Sentinel-1 image used in this study, and a total of 10 field surveys were conducted during the winter wheat growing seasons from October 2019 to February 2021. A total of 20 reference

plots were sampled in each survey. The data sampled in the field included SSM (vol.%), latitude and longitude coordinates, and the height of winter wheat at each reference plot. A TDR350 SSM meter with 3.8 cm long probes was used to measure the volumetric soil moisture content of the surface layer of the farmland. Each reference plot was sampled five times in each survey, and the average of the five measurements was taken as the actual SSM of the reference plot. At the same time, the latitude and longitude coordinates of all the reference plots in each survey were determined using an out-door handheld UG905 locator, with a positioning precision of 1 to 3 m, and recorded using the WGS84 coordinate system. The SSM measured in the field ranged from  $0.02 \text{ cm}^3/\text{cm}^3$  to  $0.29 \text{ cm}^3/\text{cm}^3$ , and the height of the wheat ranged from 0 to 48 cm throughout the field campaigns, as shown in Figure 2. More details about the utilized data characteristics were presented in Tables 1 and 2.



**Figure 2.** Main states of winter wheat growing during 10 field surveys.

**Table 2.** Information of the collected Sentinel-2 data and corresponding extracted NDVI.

Acquisition Date of Sentinel-2	Growth Stage	NDVI Range
15 October 2019	Emergence	0.08–0.15
4 November 2019	Tillering	0.16–0.34
3 January 2020	Overwintering	0.16–0.45
23 March 2020	Standing	0.51–0.72
24 October 2020	Emergence	0.12–0.47
8 November 2020	Tillering	0.20–0.58
13 December 2020	Tillering	0.38–0.71
7 January 2021	Overwintering	0.24–0.65
17 January 2021	Overwintering	0.24–0.66
16 February 2021	Standing	0.39–0.72

Finally, the dataset consisted of 200 elements. In this paper, the dataset was randomly divided into two different training and testing sets to account for the random initialization during the training of the deep learning models. In total, 80% of the 200 elements was randomly selected for model training, and the remaining 20% was used for model testing.

### 2.3. Methodology

The flow chart of the method used in this paper is shown in Figure 3. After data collection, the SSM inversion method proposed in this paper was mainly divided into 3 steps. Firstly, the feature parameters and vegetation indexes were extracted from Sentinel-1 SAR data and Sentinel-2 optical data after pre-processing, respectively. Secondly, correlation coefficient and mutual information (MI) methods were used to analyze the correlation between the extracted feature parameters and field measured SSM data to obtain the optimal combination of feature parameters. Then, the optimal combination of CNN hyper-parameters was obtained by using SSA algorithm and used to build the SSA-CNN model for SSM inversion of winter wheat covered farmlands. Finally, to demonstrate the effectiveness of the proposed SSA-CNN model, three typical machine learning models, including random forest (RF), GRNN, and CNN, were established for comparison experiments, and the regional SSM values of the study area were retrieved during 4 winter wheat phenological periods.

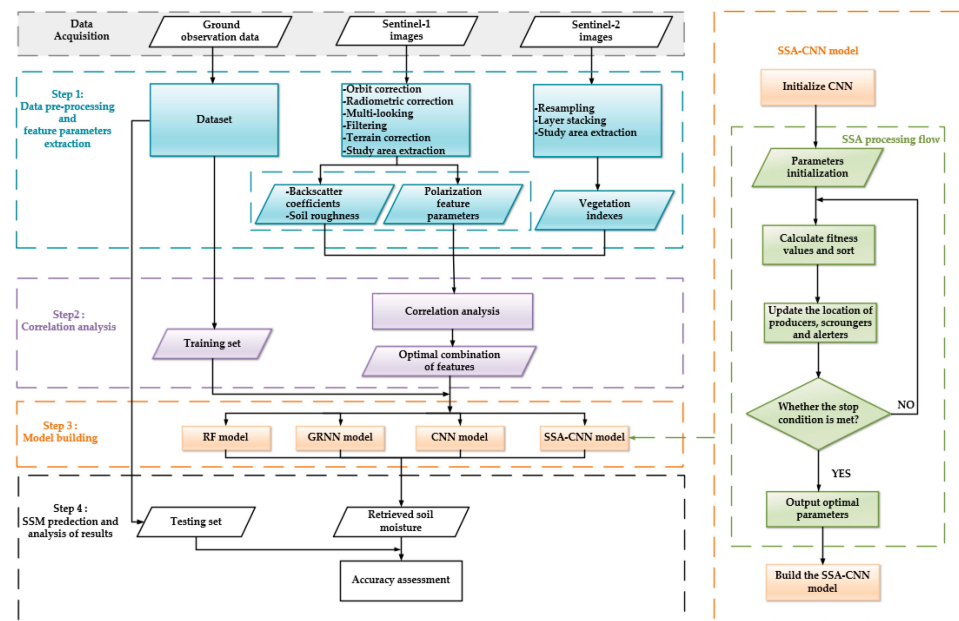


**Figure 3.** Technology roadmap.

### 2.3.1. Feature Parameters Extraction

Active microwave remote sensing emits electromagnetic waves to the surface features by radar and then receives scattered information reflected back from the surface feature. The received echo signal is different due to the different radar parameters and ground surface parameters. Meanwhile, the presence of vegetation affects the scattering of radar signals. Extracting feature information that characterizes ground objects from radar data plays an important role in radar remote sensing inversion.

- Feature Parameters Extracted from SAR Data

Firstly, using the information reflected by backscatter coefficients is the primary method of active microwave remote sensing for SSM retrieval. The incident angle ( $\theta$ ), VV, and VH polarization backscattering coefficients are extracted from the pre-processed SAR data. Secondly, the polarized scattering characteristics of SAR images can reflect the texture, roughness, and geometry of the surface features, which can help to understand and describe the scattering mechanism of the surface features. Based on the eigenvectors of the coherent matrix, the H/A/ $\alpha$  decomposition method proposed by Cloude and Pottier is an effective polarization feature parameter extraction method that is not limited to specific applications [38]. Therefore, the H/A/ $\alpha$  decomposition method was applied to the dual-polarized Sentinel-1 data to decompose the eigenvalues of the covariance matrix of the target features, from which the scattering entropy (H), inverse entropy (A), scattering angle ( $\alpha$ ), and the eigenvalues ( $\lambda_1, \lambda_2$ ) were extracted in this paper.

Thirdly, it is tough to simulate surface roughness since the information about surface roughness changes on the band frequency, the incidence angle, and the polarization mode. A combined roughness model was created from SAR data based on the existing research hypothesis that there was a correlation between surface roughness and cross-polarized backscattering coefficient [39], as shown in Equations (1)–(3).

$$Z_s = \exp\left(\frac{\sigma_{VH}^0 - \sigma_{VV}^0 - B(\theta)}{A(\theta)}\right) \quad (1)$$

$$A = -2.6408 \sin^3(\theta) + 5.293 \sin^2(\theta) - 3.838 \sin(\theta) + 2.2042 \quad (2)$$

$$B = 4.1522 \sin^3(\theta) - 13.1 \sin^2(\theta) + 16.9472 \sin(\theta) - 16.4228 \quad (3)$$

where  $Z_s$  represents the combined roughness; and  $A(dB)$  and  $B(dB)$  represent the coefficients that are related to the incident angle. They are only applicable to the combined roughness model for SAR data collected in the C-band. To sum up, a total of 9 feature parameters, as shown in Table 3, were extracted from the Sentinel-1 SAR data.

**Table 3.** Feature parameters extracted from Sentinel 1 SAR data.

No.	Parameter	Note
1	$\theta$	Incident angle
2	VV	Backscatter coefficients
3	VH	
4	H	
5	A	Inverse entropy
6	$\alpha$	Scattering angle
7	$\lambda_1$	Eigenvalues
8	$\lambda_2$	
9	$Z_s$	Surface roughness

- Feature Parameters Extracted from Optical Images

SSM distribution is influenced by vegetation coverage. It is necessary to take into account the influence of the vegetation factor in SSM inversion. Based on the spectral characteristics of the vegetation, the vegetation index is calculated by combining the visible and near-infrared bands obtained by the multispectral camera [40]. Due to the variability of surface environments in different regions and the different vegetation growth conditions in the same region, different vegetation indexes have different effects [41]. Hence, 4 commonly used vegetation indexes, including NDVI, MSI, FVI and NDWI, as shown in Table 4, were selected to eliminate the influence of vegetation coverage in this study.

**Table 4.** Vegetation indexes calculated from Sentinel-2 data.

Vegetation Index	Formulae	Reference
Normalized difference vegetation index (NDVI)	$NDVI = \frac{\rho_{NIR} - \rho_{RED}}{\rho_{NIR} + \rho_{RED}}$	[42]
Moisture stress index (MSI)	$MSI = \frac{\rho_{SWIR}}{\rho_{NIR}}$	[43]
Fusion vegetation index (FVI)	$FVI = \frac{2 * \rho_{NIR} - \rho_{RED} - \rho_{SWIR}}{2 * \rho_{NIR} + \rho_{RED} + \rho_{SWIR}}$	[44]
Normalized difference water index (NDWI)	$NDWI = \frac{\rho_{NIR} - \rho_{SWIR}}{\rho_{NIR} + \rho_{SWIR}}$	[45]

where  $\rho_{NIR}$  is the near-infrared band (band-8 of Sentinel-2),  $\rho_{RED}$  is the red band (band-4 of Sentinel-2), and  $\rho_{SWIR}$  is the short-infrared band (band-11 of Sentinel-2).

### 2.3.2. Correlation Analysis between Input Parameters and Field Measured SSM Data

When using machine learning for regression fitting problems, it is significant to choose the appropriate training data. Extra input data can cause the network to converge slowly and affect the performance of the network. Hence, when selecting training data, the feature parameters with strong correlation with field measured SSM data were selected as the import data of the model to enhance the performance of the model. In this paper, two methods, which were the correlation coefficient method and MI method, were selected to analyze the correlation between the feature parameters and field measured SSM data to reduce the dissenting nature of the correlation analysis results.

The Pearson correlation coefficient, which measures the linear correlation between two variables  $X$  and  $Y$  and is defined as shown in Equation (4), is the most often used correlation coefficient. Its value is between  $-1$  and  $1$ , and the stronger the correlation between the two variables the higher the absolute value is.

$$\rho_{X,Y} = \frac{Cov(X,Y)}{\sqrt{D(X)}\sqrt{D(Y)}} = \frac{E(X - EX)E(Y - EY)}{\sqrt{D(X)}\sqrt{D(Y)}} \quad (4)$$

where  $X$  and  $Y$  are two independent variables,  $\sqrt{D}$  represents the standard deviation,  $Cov(X,Y)$  is called the covariance of the sum of random variables,  $E$  represents the mathematical expectation, and  $\rho_{X,Y}$  represents the correlation coefficient between  $X$  and  $Y$ .

MI is an indicator of the amount of information shared between two or more variables, a measure of interdependence between random variables in information theory, and also a sensitivity analysis method used to analyze arbitrary relationships between each feature and its label, including linear and nonlinear relationships [46]. The MI of two discrete random variables  $X$  and  $Y$  can be expressed as shown in Equation (5).

$$MI(X,Y) = \sum_{x \in X} \sum_{y \in Y} p(x,y) \log \frac{p(x,y)}{p(x)p(y)} \quad (5)$$

where  $MI(X,Y)$  is called mutual information,  $p(x,y)$  represents the joint probability distribution function, and  $p(x)$  and  $p(y)$  represent the marginal probability distribution functions. The logarithm is in base 2, and the unit of mutual information is bit.

MI has many properties, two commonly used of which are symmetry and non-negativity. The normalized MI (NMI) with a value range of (0, 1) was used in this study. The larger value of NMI means more information about Y (or X) when X (or Y) is known. More information about MI is shown in [47].

In this study, a total of 13 feature parameters were selected for correlation analysis with field measured SSM data through preprocessing and analysis. By comparing the results of the above two correlation analyses, the appropriate method of correlation analysis was selected to obtain the feature parameters highly related to field measured SSM data as the optimal feature combination input of the subsequent models.

### 2.3.3. Establishment of the Models

- Traditional Machine Learning Models

GRNN is a feed forward neural network developed by Specht [48]. It consists of an input layer, a pattern layer, a summation layer, and an output layer. It is shown that this network has advantages for small sample prediction and is suitable for solving nonlinear problems. It is robust, highly fault-tolerant, and converges quickly. It can also handle unstable data. Equation (6) provides an expression for the GRNN's prediction function.

$$Y(x) = \frac{\sum_{i=1}^n y_i \exp\left[-(x - x_i)^T \cdot (x - x_i) / 2\sigma^2\right]}{\sum_{i=1}^n \exp\left[-(x - x_i)^T \cdot (x - x_i) / 2\sigma^2\right]} \quad (6)$$

where  $n$  represents the number of samples,  $x$  represents the measurement input value, and  $\sigma$  represents the smoothing factor.

RF, proposed by Leo Breiman in 2001 [49], is an integrated learning model with decision trees as the basic classifier. It uses random selection of variables and random subsets of the dataset for each decision tree to build many decision trees, and the ensemble approach can significantly improve the predictive performance of the model. RF is mainly based on Bagging and random subspaces and is used in regression problems to explain the effects of a series of independent variables on dependent variables.

The two models mentioned above, which are typical machine learning regression prediction models, perform well when applied to small samples and are frequently employed to address the challenge of small sample regression fitting. However, both methods need a lot of computing memory and effort and perform poorly when there are many training examples. This is a typical weakness in machine learning techniques for parameter inversion.

- Convolutional Neural Network Model

CNN is a representative deep learning model proposed by Lecun et al. in 1998 [50,51]. In the field of remote sensing, CNN is mainly used in surface feature recognition and image classification. However, with the in-depth study of CNN, it was found that it could be used not only for classification and target recognition but also for regression analysis. Generally speaking, input layers, convolution layers, pool layers, full connection layers, and softmax layers make up the majority of the CNN structure. The convolutional layer is used for feature learning, abstracting, and extracting features from the input data. The convolutional outputs are compressed in the pooling layer to obtain more significant features and to successfully manage overfitting. The full connection layer is used to integrate the highly abstracted features after multiple convolutions, normalize them, and send the output values to the classifier for classification. In this paper, regression function was used to replace the last softmax layer in parametric regression modeling.

Before using CNN for regression prediction, some parameters inside the CNN need to be set in advance, which are called hyper-parameters. Selecting an optimal set of hyper-parameters can enhance the CNN regression prediction performance without changing CNN structure. Therefore, it is especially important to select the suitable hyper-parameters to fully exploit the regression prediction performance of CNN architecture.

- Implementation of SSA-CNN

SSA is an emerging meta-heuristic algorithm proposed in 2020 [37]. The algorithm is simple to implement and has the advantages of high merit-seeking ability and fast convergence. In SSA, the sparrow population is divided into producers, scroungers, and alerters, and the position of each sparrow corresponds to a solution. According to the algorithm, producers and scroungers are interchangeable, but the ratio remains constant. The number of alerters is generally 10–20% of the population. In this paper, the optimal combination of hyper-parameters for the CNN model was sought using the SSA optimization algorithm. These hyper-parameters were learning rate, number of iterations, batch size, kernel size, number of convolutional layers, and number of neurons in the full connection layers. The mean square error (MSE) of the predicted and actual values was used as the fitness function with the fitness function. Then, the optimal CNN model was established using the optimal hyper-parameters, as shown in Figure 4, where the values of  $c_x$ ,  $m_x$ , and  $n_x$  were calculated by the SSA algorithm. The pooling layers were removed from the network to prevent a decline in regression prediction accuracy brought on by the loss of features from the pooled data. The gradient vanishing problem, which is especially significant when adopting saturated activation functions such as Tanh and Sigmod, is the main problem with deep learning. The ReLu function overcomes the gradient vanishing problem and accelerates the training speed [52]. The activation function was decided to be the ReLu function. For parameters inversion and prediction, the classification layer in this paper was replaced by regression layer. To avoid overfitting and enhance the generalization capabilities of the model, each fully connected layer was connected to a dropout layer.

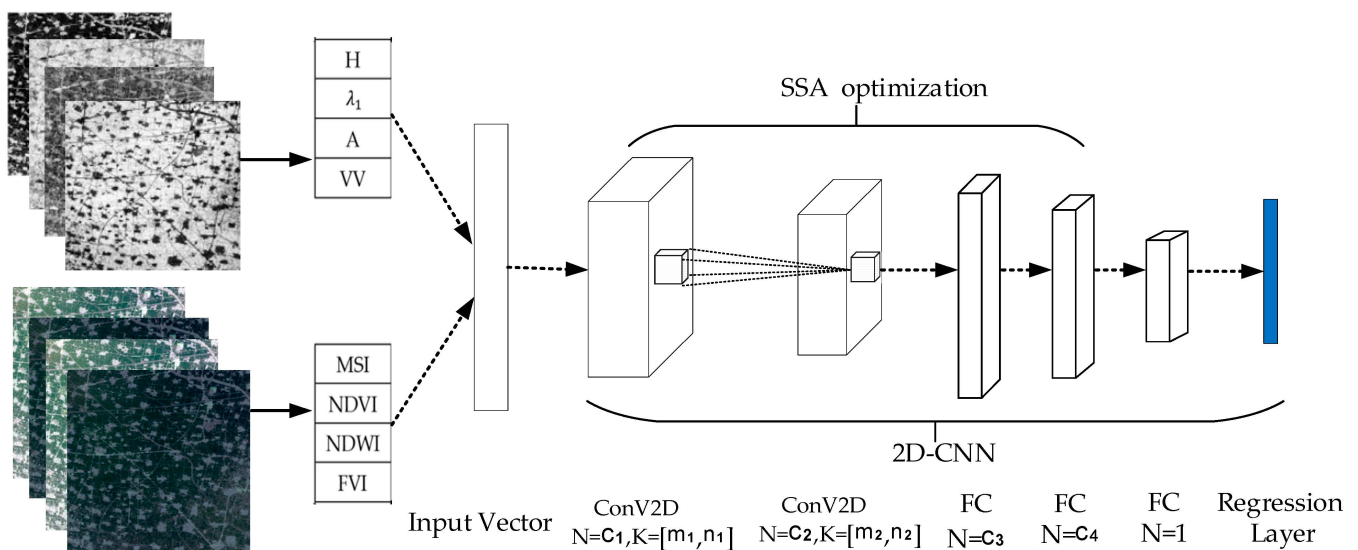


**Figure 4.** Structure of the proposed SSA-CNN model.

### 3. Results

In this section, the results of correlation analysis were first analyzed and ranked. Then, the optimal hyper-parameters combination of CNN optimized by SSA algorithm was shown. After that, RF, GRNN, CNN and SSA-CNN models were used to conduct regression modeling analysis on the datasets. At last, the optimal regression prediction model was used to invert the SSM in the study area.

#### 3.1. Correlation Analysis Results

The correlation analysis results using Pearson correlation analysis and mutual information methods are shown in Tables 5 and 6, respectively. Comparing the results of the two correlation analyses, it can be seen that the results obtained using mutual information method had a smaller variability, lower values for each feature parameter and smaller

degrees of discrimination, which could not effectively identify the main sensitive feature parameters related to field measured SSM data. As a consequence, the final results of the Pearson correlation analysis were chosen as the best input data combination for the model. Based on the results of Pearson correlation analysis, the ranked feature parameters with the highest to lowest correlation with field measured SSM data were  $\lambda_1$ , FVI, NDVI, MSI, NDWI, H, VV, A,  $\alpha$ ,  $\lambda_2$ ,  $\theta$ ,  $Z_s$ , and VH. The correlation between the four vegetation indexes and field measured SSM data was relatively high, which was due to the fact that the wavelength of 400–2500 nm had evident changes in the physiological conditions of the crops. In agricultural applications, the red band, near-infrared band, and short-wave infrared band are often used to study the biological indicators of vegetation. The biological indicators and growth conditions of these vegetation are closely related to SSM. When the growth of crops is abnormal, the changes can be reflected by the vegetation index [53]. For  $\alpha$ ,  $Z_s$ ,  $\lambda_2$ ,  $\theta$ , and VH, the correlation coefficients of these five feature parameters were less than 0.3, and they were considered to be extremely weakly correlated or uncorrelated with field measured SSM data. To summarize, the chosen eight feature parameters for the model input from high to low were  $\lambda_1$ , FVI, NDVI, MSI, NDWI, H, VV, and A.

**Table 5.** Pearson correlation coefficients ordering of feature parameters.

No.	Parameter	Correlation Coefficient
1	$\lambda_1$	0.491 **
2	FVI	−0.392 *
3	NDVI	−0.39 *
4	MSI	0.386 *
5	NDWI	−0.374 *
6	H	−0.322 *
7	VV	0.32 *
8	A	0.317 *
9	$\alpha$	−0.196
10	$\lambda_2$	0.172
11	$\theta$	−0.152
12	$Z_s$	−0.126
13	VH	0.054

The symbols \* and \*\* represent significant correlations at the 0.05 and 0.01 levels, respectively.

**Table 6.** Mutual information ordering of feature parameters.

No.	Parameter	NMI
1	$\lambda_1$	0.347
2	FVI	0.231
3	NDWI	0.228
4	MSI	0.222
5	NDVI	0.192
6	A	0.191
7	VV	0.191
8	H	0.184
9	VH	0.182
10	$\alpha$	0.172
11	$Z_s$	0.170
12	$\lambda_2$	0.165
13	$\theta$	0.147

### 3.2. Hyper-Parameters Optimization Results after SSA

The initialized structure of the CNN in this study mainly consisted of two convolutional layers, three fully connected layers, and one regression layer. Each convolutional and fully connected layer was connected to the ReLU function. The experiments of the hyper-parameter optimization using the SSA algorithm were repeated twice in this study. Every time, the dataset with 200 samples was randomly divided into a training set with

160 samples and a testing set with 40 samples. The SSA algorithm was applied twice to optimize the hyper-parameters of the same initialized CNN structure using two different training sets, and two optimal hyper-parameter combinations were obtained, as shown in Table 7.

**Table 7.** Hyper-parameters of CNN and SSA-CNN models in two repeated experiments.

Hyper-Parameter		First Training Set		Second Training Set
		CNN	SSA-CNN	SSA-CNN
Learning rate		0.01	0.006	0.004
Iterations		40	51	49
Batchsize		110	123	134
First layer	kernel size	3 × 3	3 × 3	2 × 2
First layer	number	4	5	6
Second layer	kernel size	3 × 3	2 × 2	2 × 2
Second layer	number	8	12	12
Number of neurons		30, 30, 1	32, 23, 1	31, 26, 1

### 3.3. Regression Model Results and Analysis

The RF, GRNN, and CNN models for the SSM inversion were established separately to compare with the proposed SSA-CNN model. The optimal combination of feature parameters was used as the same input data for all the four models. Three precision evaluation indexes, which were coefficient of determination ( $R^2$ ), root mean square error (RMSE), and mean absolute error (MAE), were used to evaluate the inversion accuracy. The experimental results using the two different testing sets are shown in Figures 5 and 6. It can be seen that the CNN model had higher inversion accuracy compared to the RF and GRNN models. By calculating the average accuracy of the inversion results using the two different testing sets, the average  $R^2$  of the CNN model was 0.72, the average RMSE was 2.55 vol.%, and the average MAE was 2.07 vol.%. After hyper-parameter optimization, the proposed SSA-CNN model had a further higher inversion accuracy than the CNN model, with the average  $R^2$  increasing from 0.72 to 0.80, the average RMSE decreasing from 2.55 vol.% to 2.17 vol.%, and the average MAE decreasing from 2.07 vol.% to 1.68 vol.%.

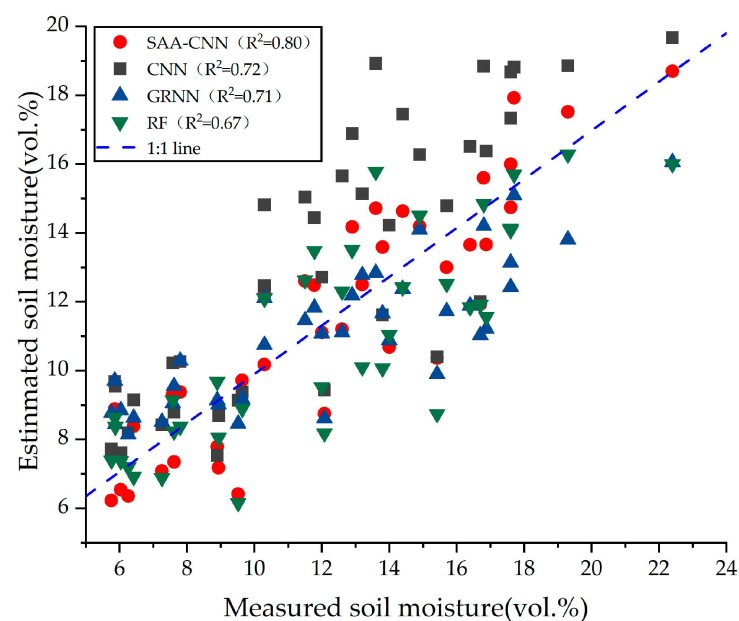


**Figure 5.** SSM prediction results for the four models using the first testing set.

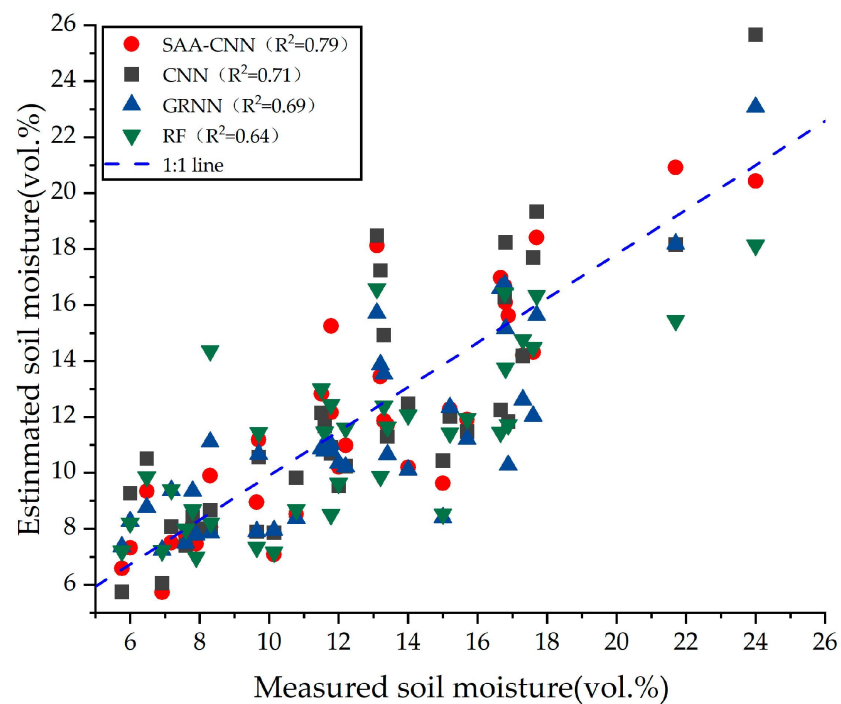


**Figure 6.** SSM prediction results for the four models using the second testing set.

The estimated accuracy of the SSM inversion results using the two different testing sets is shown in Table 8. It is shown that the SSM inversion results of the proposed SSA-CNN model were much closer to the ground-truth values, compared with the other three models. The results indicated that the SSM inversion accuracy could be improved by using SSA algorithm to optimize the hyper-parameters of the CNN model, which demonstrated the superiority of the proposed SSA-CNN model.

**Table 8.** Prediction accuracy of the four models in the two repeated experiments.

Model	First Testing Set			Second Testing Set			Average Accuracy		
	$R^2$	RMSE (Vol.%)	MAE (Vol.%)	$R^2$	RMSE (Vol.%)	MAE (Vol.%)	$R^2$	RMSE (Vol.%)	MAE (Vol.%)
SSA-CNN	0.80	2.11	1.65	0.79	2.22	1.71	0.80	2.17	1.68
CNN	0.72	2.53	2.09	0.71	2.57	2.05	0.72	2.55	2.07
GRNN	0.71	2.81	2.25	0.69	3.05	2.33	0.70	2.93	2.29
RF	0.67	2.83	2.46	0.64	3.12	2.61	0.66	2.98	2.54

### 3.4. Performance of the Four Models with Different Number of the Feature Parameters

The optimal size of the feature parameter subset used as the input data of the subsequent four models was explored in this study. The number of the used feature parameters was gradually increased to use in the four models, according to the correlation ranking of the feature parameters. First, only the top feature parameter with the highest relevance ranking was used as input data to build the four models. Then, the four models were constructed using the top two feature parameters in the correlation ranking. Finally, the number of the used feature parameters was gradually increased until all of them were used to build the four models. The result is shown in Figure 7. As can be seen in Figure 7, there was a general trend in decreasing and then increasing of the RMSEs of the four models with the increase in the number of the used feature parameters. In other words, a general trend in increasing and then decreasing of the estimation accuracy of the four models was shown with the increase in the number of feature parameters. Although the fluctuations of the four

models were not the same, it was demonstrated that the trough of the RMSE curve, which meant the highest estimation accuracy, occurred when the top eight feature parameters in the correlation ranking were used in the four models. When the number of the used feature parameters was greater than eight, the accuracy of the four models on the testing set would decrease. The above results showed that redundant feature parameters could negatively affect the fitting performance of the models to some extent. Therefore, correlation analysis before conducting models was important to eliminate redundant feature parameters and effectively improve the inversion accuracy. In addition, it was also shown in Figure 7 that the SSA-CNN model proposed in this paper had the least fluctuation in accuracy and was more stable among the four models, which further demonstrated its better performance.

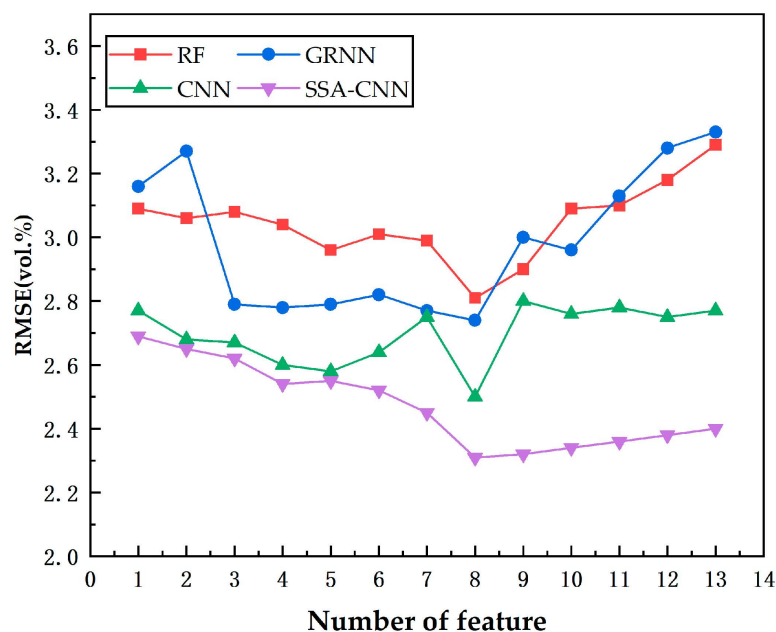


**Figure 7.** Performance of the four models with different number of the feature parameters.

### 3.5. Analysis of Soil Moisture Dynamic Changes

The dynamic change in the average SSM in the winter wheat growing period is shown in Figure 8. The average SSM values in the emergence stage, tillering stage, overwintering stage, and standing stage of the winter wheat growing periods in 2019–2020 and 2021–2021 are represented in Figure 8a,b, respectively. On the whole, it is demonstrated in Figure 8a that a decreasing trend in the average SSM was shown from the emergence stage to the overwintering stage of the winter wheat. As sufficient soil moisture content was necessary to ensure the emergence rate of winter wheat, much irrigation usually occurred during the emergence period. With the growth of wheat seedlings and the evaporation of SSM, the soil water consumption increased, and, therefore, the average SSM decreased gradually. During the standing stage of winter wheat, a slight increase in the average SSM was shown compared with that of the overwintering stage, mainly because the temperature gradually rose, and the growth rate of wheat seedlings was accelerated during the standing stage. It should be pointed out that there was an evident ascent of the average field measured SSM during the tillering stage in Figure 8b because it rained in the study area on the day before the field survey on 11 December 2020. The trend in the average SSM during the remaining phenological stages in Figure 8b was similar to that in Figure 8a. Overall, these four models tracked the dynamic changes in SSM well, and the proposed SSA-CNN model showed better performance than the other three models.

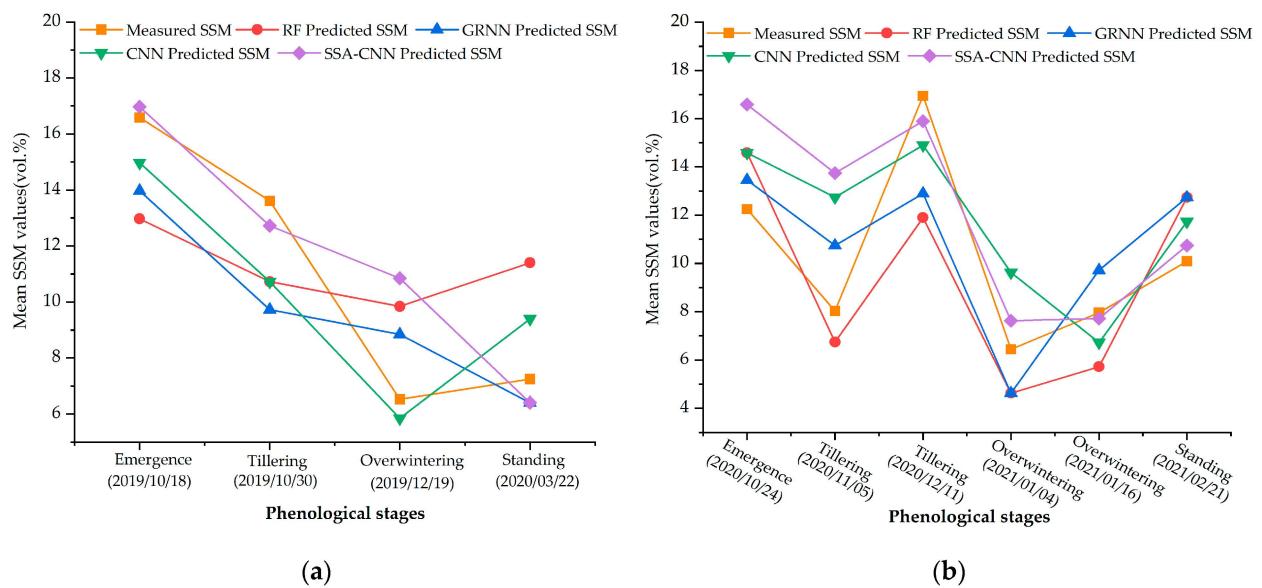


**Figure 8.** Mean SSM variation in winter wheat pre-fertility periods: (a) 2019/10/18–2020/03/22; (b) 2020/10/24–2021/02/21.

### 3.6. Performance of SSM Estimation under Different Coverages of the Winter Wheat Plants

In this study, NDVI was used as a surrogate for winter wheat biomass to judge the growth status of winter wheat. Based on the 10 Sentinel-2 images covering the study area, the average values of all the NDVIs at the sampling points in each field survey were calculated, as shown in Figure 9.

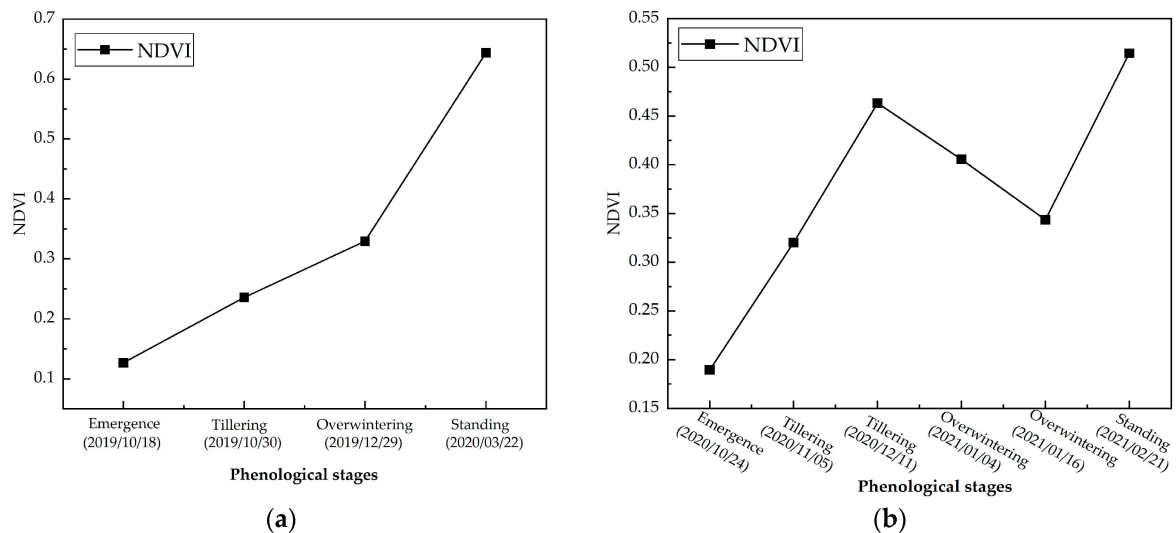


**Figure 9.** Dynamics of the mean NDVI of the winter wheat sampling sites: (a) 2019/10/18–2020/03/22; (b) 2020/10/24–2021/02/21.

It was demonstrated in Figure 9 that the NDVI exhibited an upward trend overall in each growing period and was consistent with the growth process of the winter wheat. During the periods from 15 October 2019 to 23 March 2020 and 24 October 2020 to 16 February 2021, the ground coverage density of winter wheat increased gradually as a whole; except for the overwintering stage, when the growth of winter wheat almost stopped, and the coverage of winter wheat remained almost constant. It corresponded to the increasing trend in the NDVI. It was worth noting that the winter wheat exhibited a relatively poor state, with a reduced green coverage rate, during the overwintering stage. As a result, the

red absorption band weakened, which was reflected in the downward trend in the NDVI from 13 December 2020 to 17 January 2021. A comparison of the differences in the growth status of winter wheat in the 10 field surveys is shown in Figure 2. The RMSE between the measured and estimated SSM using the 4 models at the 10 survey dates is shown in Figure 10. From Figures 9 and 10, it can be seen overall that RMSE increased accordingly with the increase in NDVI, namely, the increase in winter wheat. However, the SSA-CNN model proposed in this paper had a more stable accuracy in general compared with the other three models.

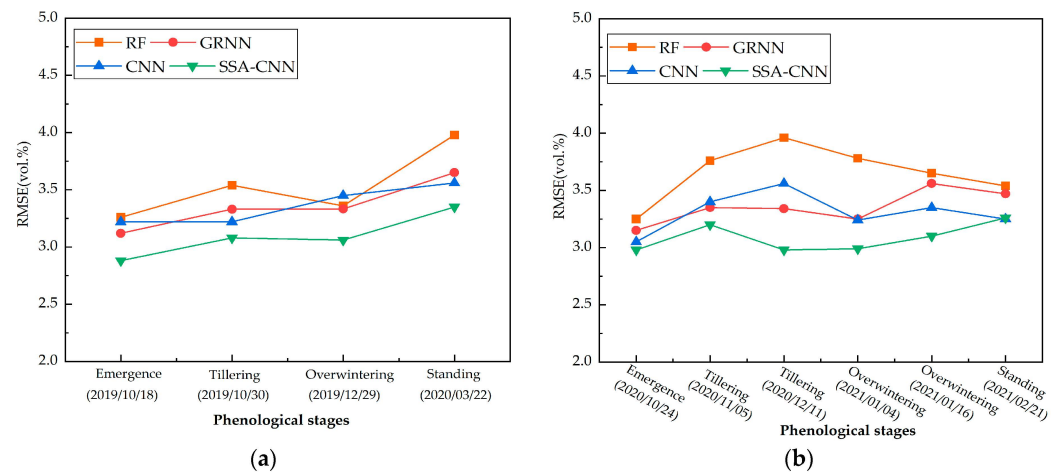


**Figure 10.** RMSE of between SSM estimated and measured on 10 dates using the four models: (a) 2019/10/18–2020/03/22; (b) 2020/10/24–2021/02/21.

3.7. Results of the Regional SSM Inversion

The proposed SSA-CNN model was used to estimate the SSM in the winter wheat covered farmlands in the study area, based on the Sentinel-1 and Sentinel-2 remote sensing data. The results are shown in Figures 11–14, which demonstrate the spatial distributions of the SSM during the four phenological stages in the first growth cycle of winter wheat and the difference analysis of the measured and retrieved SSM values at 20 reference plots in each Sentinel-1 image. The spatial distributions of the SSM in the second growth cycle of winter wheat were similar and, therefore, not repeatedly shown here. Non-farming areas such as buildings, roads, and rivers were prescreened in advance and filled with white pixels to highlight the farmland areas on the SSM distribution map.

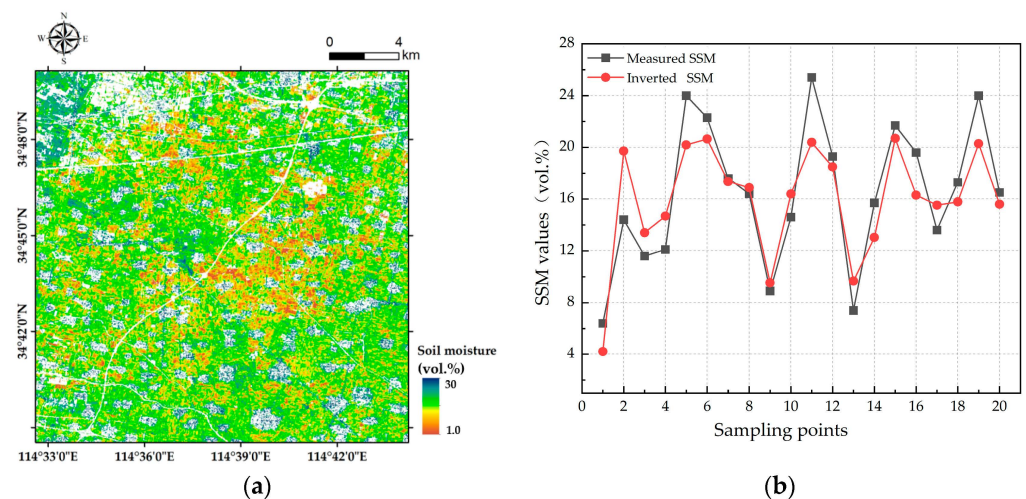


**Figure 11.** Inversion results for 18 October 2019: (a) Inversion results of the regional SSM in the study area; (b) Differences of the measured and retrieved SSM values at 20 reference plots.

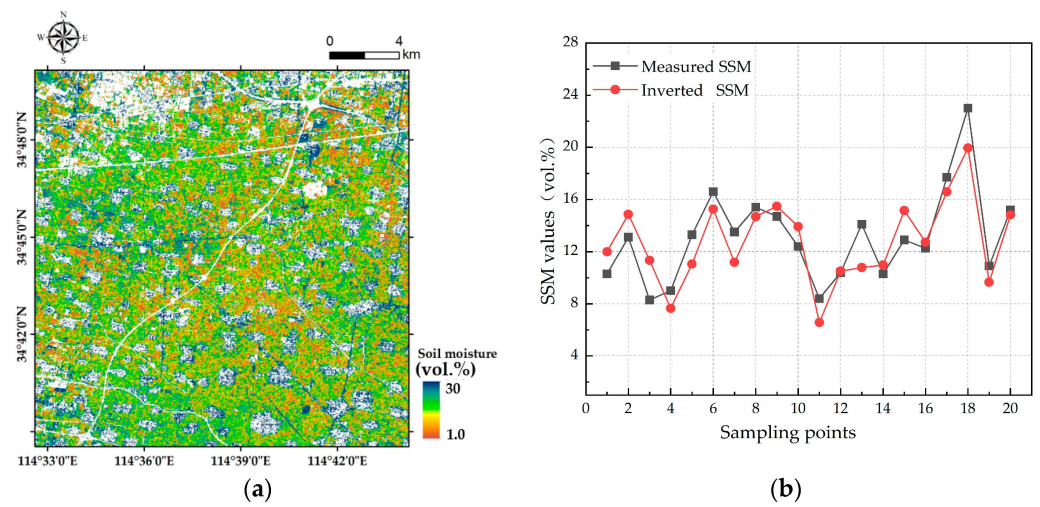


**Figure 12.** Inversion results for 30 October 2019: (a) Inversion results of the regional SSM in the study area; (b) Differences of the measured and retrieved SSM values at 20 reference plots.

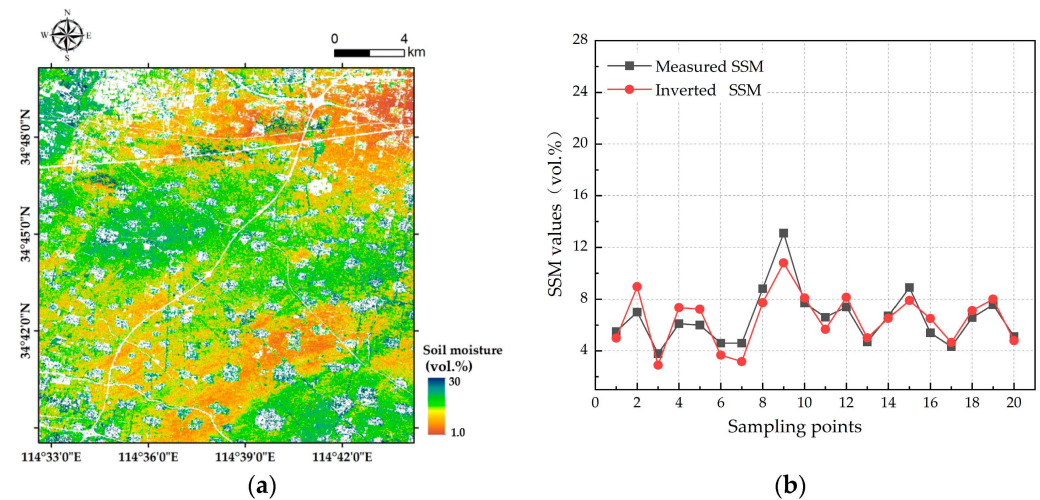


**Figure 13.** Inversion results for 29 December 2019: (a) Inversion results of the regional SSM in the study area; (b) Differences of the measured and retrieved SSM values at 20 reference plots.

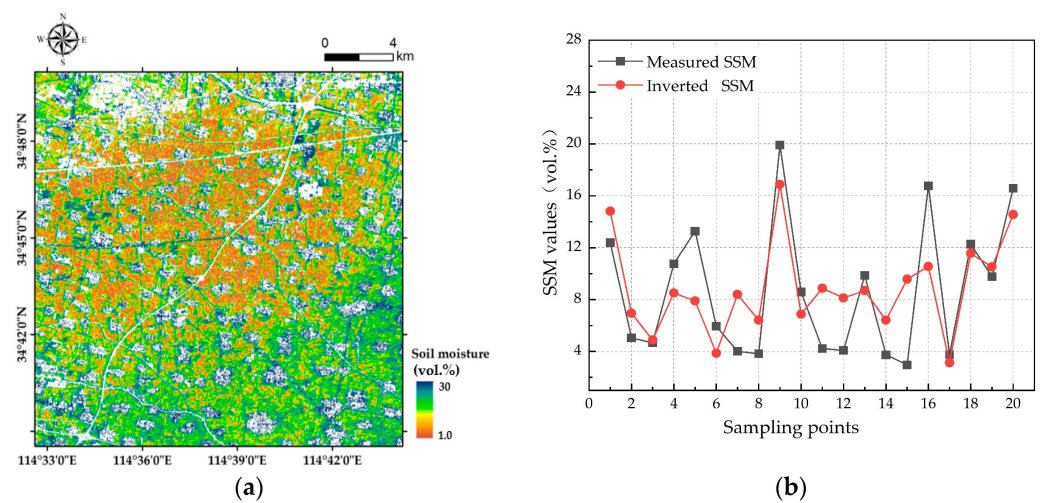


**Figure 14.** Inversion results for 22 March 2020: (a) Inversion results of the regional SSM in the study area; (b) Differences of the measured and retrieved SSM values at 20 reference plots.

From the inversion results, the SSM was relatively high in the early stage of the wheat phenological stage because the wheat seedling emergence required certain moisture in the early stage of wheat growth and development, and insufficient moisture would affect the seedling emergence rate. From Figures 11b and 14b, it can be observed that there were significant variations in SSM within the same day. This difference was mainly attributed to the fact that winter wheat during these two dates was in the critical stages of emergence and standing stages. During these two growth stages, the crop had a higher water demand, leading to more frequent irrigation activities in the fields. However, due to the possible differences in irrigation timing, methods, and intensity among the various plots within the planting area, this resulted in significant variations in SSM values expression within the same day. With the growth and development of winter wheat, its growth mainly depended on the natural precipitation in the area. With uniform rainfall in the study area, the spatial variation in SSM in the late stage of winter wheat growth was small, and the SSM gradually decreased. Especially, to demonstrate the significant effect of rainfall events on SSM values, the inversion results for 11 December 2020, the day after it rained in the study area, which was mentioned in Section 3.5, are shown in Figure 15. As can be seen from Figure 15, the SSM was generally higher after the rainfall. This was mainly due to the fact that the rainfall provided a large amount of water replenishment to the soil, allowing sufficient adsorption and infiltration of water in the soil. In conclusion, the above results showed that the inversion method proposed in this paper was feasible and applicable to the regional SSM retrieval in the winter wheat covered areas.

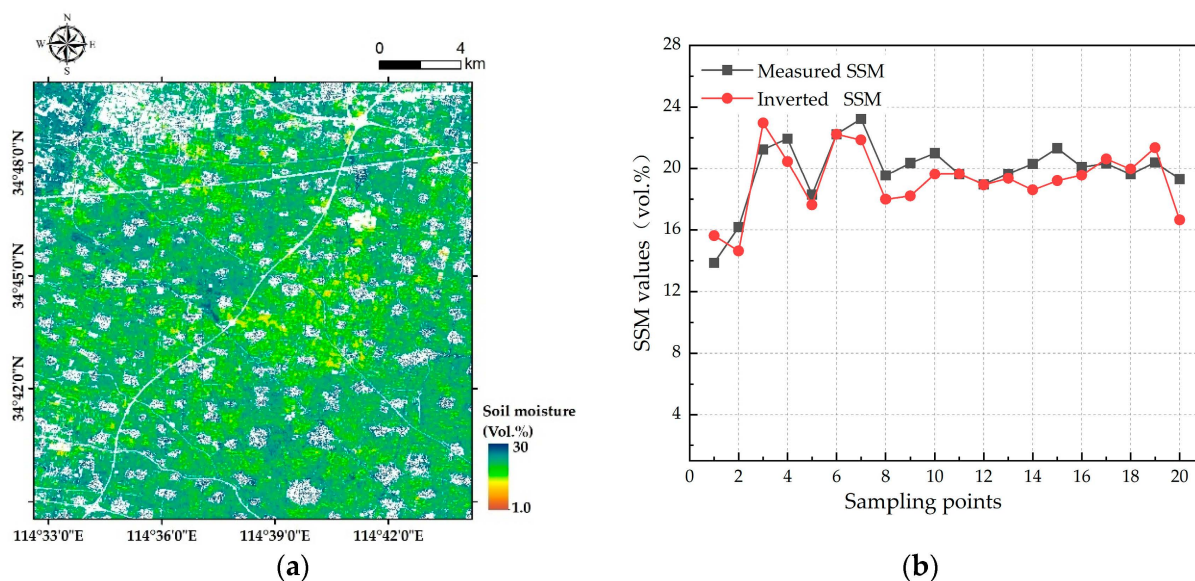


**Figure 15.** Inversion results for 11 December 2020: (a) Inversion results of the regional SSM in the study area; (b) Differences of the measured and retrieved SSM values at 20 reference plots.

#### 4. Discussion

The SSM inversion in winter wheat farmlands was investigated in this study based on Sentinel-1 and Sentinel-2 multi-source remote sensing data. Good inversion results were achieved through the optimization of the feature parameters extracted from remote sensing data and the optimization of the neural network hyper-parameters. First, the feature parameters related to the SSM in SAR images and optical images were extracted, and the Pearson correlation analysis method was used to select the optimal feature parameter subset. Then, the SSA algorithm and CNN model were combined to develop a new inversion model for SSM inversion. Finally, the quantitative and qualitative evaluation results demonstrated the effectiveness of the proposed method. Despite the fact that significant benefits were obtained through feature optimization and the development of SSA-CNN model, there are still some issues to be further discussed.

First of all, based on all the field measured SSM values collected during four phenological stages of winter wheat, the optimal combination of the feature parameters extracted from multi-source remote sensing data was selected through the correlation analysis method in this paper and uniformly used in subsequent inversion models to retrieve regional SSM during the four phenological stages of winter wheat. However, the correlation between the remote sensing feature parameters and field measured SSM of winter wheat covered area may be various in different phenological stages of winter wheat and thus is the optimal combination of remote sensing feature parameters, which needs to be further analyzed in future research.

Next, the hyper-parameters are crucial to the performance of CNN model, and different settings of hyper-parameters may lead to different generalization capabilities. Compared with the traditional manual hyper-parameter adjustment method, the experimental results showed that the SSA optimization method used in this paper was much more convenient and effective. It is worth noting that the hyper-parameter settings of the deep learning models had some inexplicable aspects, which need to be analyzed specifically for specific problems, due to the black box nature of deep learning. More hyper-parameter optimization methods suitable for SSM inversion are the focus of the subsequent research.

In the end, the performance of the proposed method was evaluated at different winter wheat coverages in this study, as shown in Figures 11–14. It can be seen from Figures 9 and 10 that the accuracy of the estimated SSM decreased with the increase in the NDVI. The reason may be that the sensitivity of radar signal to soil moisture decreases when the vegetation coverage increases [54,55]. Although the proposed method obtained satisfactory estimates of SSM in general in the pre-fertility periods of winter wheat, more improvements could be explored to further increase the inversion accuracy in the late growth periods, when the winter wheat was taller, denser, and with higher NDVI.

## 5. Conclusions

In this paper, based on Sentinel-1 SAR data and Sentinel-2 optical data, an SSM inversion method based on the SSA-CNN model, which was a convolution neural network optimized by sparrow search algorithm, was proposed to retrieve SSM in winter wheat farmlands. The following are the primary conclusions:

- (1) In total, 14 feature parameters related to SSM were extracted from Sentinel-1 and Sentinel-2 remote sensing data. After correlation analysis between 13 extracted feature parameters and field measured SSM by using Pearson correlation analysis and mutual information methods, 8 feature parameters, which were  $\lambda_1$ , FVI, NDVI, MSI, NDWI, H, VV, and A, were selected as the optimal combination of feature parameters for SSM inversion.
- (2) The SSA-CNN model was established and compared with RF, GRNN, and CNN models to validate its effectiveness. Among the four models, the proposed SSA-CNN model had a higher inversion accuracy. Its average  $R^2$ , average RMSE, and average MAE were 0.80, 2.17 vol.%, and 1.68 vol.%, respectively.
- (3) The proposed SSA-CNN model was used to retrieve the regional SSM in winter wheat farmlands during four phenological stages. The findings indicated that the proposed method was feasible and suitable for SSM inversion in winter wheat covered areas, which provided a beneficial exploration and technical support for SSM estimation in agricultural regions.

**Author Contributions:** Methodology, R.W., J.Z., H.Y. and N.L.; investigation, J.Z. and R.W.; experiment and visualization, R.W.; validation, J.Z., N.L. and H.Y.; writing—original draft, R.W. and J.Z.; writing—review and editing, R.W., J.Z., N.L. and H.Y. All authors have read and agreed to the published version of the manuscript.

**Funding:** This work was supported by the National Natural Science Foundation of China (42101386), the Plan of Science and Technology of Henan Province (212102210093, 222102110439, 212102210101), the College Key Research Project of Henan Province (22A520021, 21A520004), the Plan of Science and Technology of Kaifeng City (2102005), and the Key Laboratory of Natural Resources Monitoring and Regulation in Southern Hilly Region, Ministry of Natural Resources of the People’s Republic of China (NRMSSHR2022Z01).

**Data Availability Statement:** Not applicable.

**Acknowledgments:** The authors would like to thank the European Space Agency (ESA) for providing the Sentinel-1 and Sentinel-2 data and the anonymous reviewers and editors for their valuable comments that were crucial in improving the quality of this paper. The authors would also like to thank all the teachers and students of the SAR information processing team of Henan University for helping this study.

**Conflicts of Interest:** The authors declare no conflict of interest.

## References

- Guo, J.; Liu, J.; Ning, J.F.; Han, W.T. Construction and validation of farmland surface soil moisture retrieval model based on sentinel multi-source data. *Trans. Chin. Soc. Agric. Eng.* **2019**, *35*, 71–78.
- Gao, F.; Wang, J.M.; Sun, C.Q.; Wen, J. Progress in microwave remote sensing of soil moisture. *Remote Sens. Technol. Appl.* **2001**, *16*, 97–102.
- Zhang, X.; Chen, B.Z.; Zhao, H.; Wang, L. Based on time series Sentinel-1A data detection and analysis of farmland soil moisture change. *Remote Sens. Technol. Appl.* **2017**, *32*, 338–345.
- De Roo, R.D.; Du, Y.; Ulaby, F.T.; Dobson, M.C. A semi-empirical backscattering model at L-band and C-band for a soybean canopy with soil moisture inversion. *IEEE Trans. Geosci. Remote Sens.* **2001**, *39*, 864–872. [[CrossRef](#)]
- Verhoest, N.E.; Lievens, H.; Wagner, W.; Álvarez-Mozos, J.; Moran, M.S.; Mattia, F. On the soil roughness parameterization problem in soil moisture retrieval of bare surfaces from synthetic aperture radar. *Sensors* **2008**, *8*, 4213–4248. [[CrossRef](#)]
- Marzahn, P.; Ludwig, R. On the derivation of soil surface roughness from multi parametric PolSAR data and its potential for hydrological modeling. *Hydrol. Earth Syst. Sci.* **2009**, *13*, 381–394. [[CrossRef](#)]
- Yu, F.; Zhao, Y.S.; Li, H.T. Active passive remote sensing collaborative retrieval of soil moisture based on genetic BP neural network. *J. Infrared Millim. Waves* **2012**, *31*, 283–288. [[CrossRef](#)]
- Sandholt, I.; Rasmussen, K.; Andersen, J. A simple interpretation of the surface temperature/vegetation index space for assessment of surface moisture status. *Remote Sens. Environ.* **2002**, *79*, 213–224. [[CrossRef](#)]
- Yang, J.H.; Chen, L.W.; Wang, Y.X.; Zhao, S.X. Inversion of soil moisture based on improved water cloud model. *Technol. Innov. Appl.* **2020**, *10*, 13–15.
- Al-Yaari, A.; Wigneron, J.P.; Ducharne, A.; Kerr, Y.; De Rosnay, P.; De Jeu, R.; Mialon, A. Global-scale evaluation of two satellite-based passive microwave soil moisture datasets (SMOS and AMSR-E) with respect to Land Data Assimilation System estimates. *Remote Sens. Environ.* **2014**, *149*, 181–195. [[CrossRef](#)]
- Zhu, J.; Tsang, L.; Liao, T.H. Remote Sensing of Deep Snow with C Band Radar Data: Volume and Surface Scattering. In Proceedings of the 2021 IEEE International Geoscience and Remote Sensing Symposium IGARSS, Brussels, Belgium, 11–16 July 2021; IEEE: Piscataway, NJ, USA, 2021; pp. 622–624.
- Zhang, M. Surface Soil Moisture Retrieval in Wheat Covered Area Using Multi-Temporal SAR and Optical Satellite Data. Master’s Thesis, China University of Mining and Technology, Xuzhou, China, 2021.
- Bai, X.J. Research on Methods for Soil Moisture Retrieval in Prairies Areas Based on Multi-Frequency and Multi-Polarization SAR Data. Ph.D. Thesis, University of Electronic Science and Technology of China, Chengdu, China, 2017.
- Wang, S.N.; Li, R.P.; Wu, Y.J.; Zhao, S.X.; Wang, X.Q. Soil moisture retrieval based on environmental variables and machine learning. *Trans. Chin. Soc. Agric. Mach.* **2022**, *53*, 332–341.
- Chen, L.; Xing, M.; He, B.; Wang, J.; Shang, J.; Huang, X.; Xu, M. Estimating soil moisture over winter wheat fields during growing season using machine-learning methods. *IEEE J. Sel. Top. Appl. Earth Obs. Remote Sens.* **2021**, *14*, 3706–3718. [[CrossRef](#)]
- Karthikeyan, L.; Pan, M.; Wanders, N.; Kumar, D.N.; Wood, E.F. Four decades of microwave satellite soil moisture observations: Part 1. A review of retrieval algorithms. *Adv. Water Resour.* **2017**, *109*, 106–120. [[CrossRef](#)]
- Petropoulos, G.P.; Ireland, G.; Barrett, B. Surface soil moisture retrievals from remote sensing: Current status, products & future trends. *Phys. Chem. Earth* **2015**, *83*, 36–56.
- Callens, M.; Verhoest, N.E.C.; Davidson, M.W.J. Parameterization of tillage-induced single-scale soil roughness from 4-m profiles. *IEEE Trans. Geosci. Remote Sens.* **2006**, *44*, 878–888. [[CrossRef](#)]
- Jagdhuber, T.; Hajnsek, I.; Papathanassiou, K.P. An iterative generalized hybrid decomposition for soil moisture retrieval under vegetation cover using fully polarimetric SAR. *IEEE J. Sel. Top. Appl. Earth Obs. Remote Sens.* **2014**, *8*, 3911–3922. [[CrossRef](#)]
- Hajnsek, I.; Pottier, E.; Cloude, S.R. Inversion of surface parameters from polarimetric SAR. *IEEE Trans. Geosci. Remote Sens.* **2003**, *41*, 727–744. [[CrossRef](#)]

21. Ulaby, F.T.; Batlivala, P.P.; Dobson, M.C. Microwave backscatter dependence on surface roughness, soil moisture, and soil texture: Part I-bare soil. *IEEE Trans. Geosci. Electron.* **1978**, *16*, 286–295. [[CrossRef](#)]
22. Oh, Y.; Sarabandi, K.; Ulaby, F.T. An empirical model and an inversion technique for radar scattering from bare soil surfaces. *IEEE Trans. Geosci. Remote Sens.* **1992**, *30*, 370–381. [[CrossRef](#)]
23. Dobson, M.C.; Ulaby, F.T. Active microwave soil moisture research. *IEEE Trans. Geosci. Remote Sens.* **1986**, *1*, 23–36. [[CrossRef](#)]
24. Shi, J.; Wang, J.; Hsu, A.Y.; O’Neill, P.E.; Engman, E.T. Estimation of bare surface soil moisture and surface roughness parameter using L-band SAR image data. *IEEE Trans. Geosci. Remote Sens.* **1997**, *35*, 1254–1266.
25. Ulaby, F.T.; Sarabandi, K.; McDonald, K.Y.L.E.; Whitt, M.; Dobson, M.C. Michigan microwave canopy scattering model. *Int. J. Remote Sens.* **1990**, *11*, 1223–1253. [[CrossRef](#)]
26. Attema, E.P.W.; Ulaby, F.T. Vegetation modeled as a water cloud. *Radio Sci.* **1978**, *13*, 357–364. [[CrossRef](#)]
27. Bousbih, S.; Zribi, M.; Mougenot, B.; Fanise, P.; Lili-Chabaane, Z.; Baghdadi, N. Monitoring of surface soil moisture based on optical and radar data over agricultural fields. In Proceedings of the 2018 4th International Conference on Advanced Technologies for Signal and Image Processing (ATSIP), Sousse, Tunisia, 21–24 March 2018; IEEE: Piscataway, NJ, USA, 2018; pp. 1–5.
28. El Hajj, M.; Baghdadi, N.; Zribi, M.; Bazzi, H. Synergic use of Sentinel-1 and Sentinel-2 images for operational soil moisture mapping at high spatial resolution over agricultural areas. *Remote Sens.* **2017**, *9*, 1292. [[CrossRef](#)]
29. Tong, C.; Wang, H.; Magagi, R.; Goita, K.; Zhu, L.; Yang, M.; Deng, J. Soil moisture retrievals by combining passive microwave and optical data. *Remote Sens.* **2020**, *12*, 3173. [[CrossRef](#)]
30. Ali, I.; Greifeneder, F.; Stamenkovic, J.; Neumann, M.; Notarnicola, C. Review of machine learning approaches for biomass and soil moisture retrievals from remote sensing data. *Remote Sens.* **2015**, *7*, 16398–16421. [[CrossRef](#)]
31. Grewal, D.S. A critical conceptual analysis of definitions of artificial intelligence as applicable to computer engineering. *IOSR J. Comput. Eng.* **2014**, *16*, 9–13. [[CrossRef](#)]
32. Vasconcelos, L.; Kijanka, P.; Urban, M.W. Viscoelastic parameter estimation using simulated shear wave motion and convolutional neural networks. *Comput. Biol. Med.* **2021**, *133*, 104382. [[CrossRef](#)]
33. Liu, J.; Xu, Y.; Li, H.; Guo, J. Soil moisture retrieval in farmland areas with sentinel multi-source data based on regression convolutional neural networks. *Sensors* **2021**, *21*, 877. [[CrossRef](#)]
34. Song, X.; Tang, L.; Zhao, S.; Zhang, X.; Li, L.; Huang, J.; Cai, W. Grey Wolf Optimizer for parameter estimation in surface waves. *Soil. Dyn. Earthq. Eng.* **2015**, *75*, 147–157. [[CrossRef](#)]
35. Rashedi, E.; Nezamabadi-Pour, H.; Saryazdi, S. GSA: A Gravitational Search Algorithm. *Inf. Sci.* **2009**, *179*, 2232–2248. [[CrossRef](#)]
36. Poli, R.; Kennedy, J.; Blackwell, T. Particle swarm optimization. *Swarm Intell.* **2007**, *1*, 33–57. [[CrossRef](#)]
37. Xue, J.; Shen, B. A novel swarm intelligence optimization approach: Sparrow search algorithm. *Syst. Sci. Control Eng.* **2020**, *8*, 22–34. [[CrossRef](#)]
38. Cloude, S.R.; Pottier, E. An entropy based classification scheme for land applications of polarimetric SAR. *IEEE Trans. Geosci. Remote Sens.* **1997**, *35*, 68–78. [[CrossRef](#)]
39. Tong, L.; Chen, Y.; Jia, M.Q. *Mechanism of Radar Remote Sensing*; Science Press: Beijing, China, 2014.
40. Huang, S.; Tang, L.; Hupy, J.P.; Wang, Y.; Shao, G. A commentary review on the use of normalized difference vegetation index (NDVI) in the era of popular remote sensing. *J. For. Res.* **2021**, *32*, 1–6. [[CrossRef](#)]
41. Liu, J. Soil Moisture Retrieval in Farmland Surface Based on Sentinel Multi-Source Remote Sensing Data. Master’s Thesis, Northwest A&F University, Yangling, China, 2020.
42. Qi, J.; Chehbouni, A.; Huete, A.R.; Kerr, Y.H.; Sorooshian, S. A modified soil adjusted vegetation index. *Remote Sens. Environ.* **1994**, *48*, 119–126. [[CrossRef](#)]
43. Zhao, X.; Wang, J.; Liu, S. Improved monitoring of vegetation water content by remote sensing with coupled radiative transfer model. *J. Infrared Millim. Waves* **2010**, *29*, 185–189. [[CrossRef](#)]
44. Zhao, J.; Zhang, B.; Li, N.; Guo, Z. Synergistic inversion of soil moisture on winter wheat cover surface based on Sentinel-1/2 remote sensing data. *J. Electron. Inf. Technol.* **2021**, *43*, 692–699.
45. McFeeters, S.K. The use of the Normalized Difference Water Index (NDWI) in the delineation of open water features. *Int. J. Remote Sens.* **1996**, *17*, 1425–1432. [[CrossRef](#)]
46. Xiong, J.Z. Urban Stormwater Model Parameter Sensitivity Analysis and Calibration. Master’s Thesis, Shandong University, Jinan, China, 2016.
47. Hu, Q.; Guo, M.; Yu, D.; Liu, J. Information entropy for ordinal classification. *Sci. China Inf. Sci.* **2010**, *53*, 1188–1200. [[CrossRef](#)]
48. Specht, D.F. A general regression neural network. *IEEE. Trans. Neural Networ.* **1991**, *2*, 568–576. [[CrossRef](#)] [[PubMed](#)]
49. Breiman, L. Random forests. *Mach. Learn.* **2001**, *45*, 5–32. [[CrossRef](#)]
50. LeCun, Y.; Bottou, L.; Bengio, Y.; Haffner, P. Gradient-based learning applied to document recognition. *Proc. IEEE* **1998**, *86*, 2278–2324. [[CrossRef](#)]
51. Zhong, L.; Hu, L.; Zhou, H. Deep learning based multi-temporal crop classification. *Remote Sens. Environ.* **2019**, *221*, 430–443. [[CrossRef](#)]
52. Guo, J.; Bai, Q.; Guo, W.; Bu, Z.; Zhang, W. Soil moisture content estimation in winter wheat planting area for multi-source sensing data using CNNR. *Comput. Electron. Agr.* **2022**, *193*, 106670. [[CrossRef](#)]
53. Fu, Y.Z. Study on Vegetation Index of Remote Sensing and Its Applications. Master’s Thesis, Fuzhou University, Fuzhou, China, 2010.

54. Baghdadi, N.; EL Hajj, M.; Zribi, M.; Fayad, I. Coupling SAR C-Band and Optical Data for Soil Moisture and Leaf Area Index Retrieval Over Irrigated Grasslands. *IEEE J. Sel. Top. Appl. Earth Obs. Remote Sens.* **2015**, *9*, 1229–1243.
55. El Hajj, M.; Baghdadi, N.; Belaud, G.; Zribi, M.; Cheviron, B.; Courault, D.; Hagolle, O.; Charron, F. Irrigated grassland monitoring using a time series of terraSAR-X and COSMO-skyMed X-Band SAR Data. *Remote Sens.* **2014**, *6*, 10002–10032. [[CrossRef](#)]

**Disclaimer/Publisher’s Note:** The statements, opinions and data contained in all publications are solely those of the individual author(s) and contributor(s) and not of MDPI and/or the editor(s). MDPI and/or the editor(s) disclaim responsibility for any injury to people or property resulting from any ideas, methods, instructions or products referred to in the content.